

## Hyperthermia with rotating magnetic nanowires inducing heat into tumor by fluid friction

Peter W. Egolf,<sup>1</sup> Naveen Shamsudhin,<sup>2,a)</sup> Salvador Pané,<sup>2</sup> Didier Vuarnoz,<sup>3</sup> Juho Pokki,<sup>2</sup> Anne-Gabrielle Pawlowski,<sup>1</sup> Paulin Tsague,<sup>1</sup> Bastien de Marco,<sup>1</sup> William Bovy,<sup>1</sup> Sinisa Tucev,<sup>1</sup> M. H. D. Ansari,<sup>2</sup> and Bradley J. Nelson<sup>2</sup>

<sup>1</sup>Institute of Thermal Sciences and Engineering, University of Applied Sciences of Western Switzerland, CH 1401 Yverdon-les-Bains, Switzerland

<sup>2</sup>Multi-Scale Robotics Lab, Institute of Robotics and Intelligent Systems, ETH Zurich, CH 8092 Zurich, Switzerland

<sup>3</sup>Ecole Polytechnique Fédérale de Lausanne (EPFL), EPFL Fribourg, CH 1701 Fribourg, Switzerland

(Received 18 February 2016; accepted 23 July 2016; published online 9 August 2016)

A magnetic hyperthermia cancer treatment strategy that does not operate by means of conventional heating mechanisms is presented. The proposed approach consists of injecting a gel with homogeneously distributed magnetic nanowires into a tumor. Upon the application of a *low-frequency* rotating or circularly polarized magnetic field, nanowires spin around their center of viscous drag due to torque generated by shape anisotropy. As a result of external rotational forcing and fluid friction in the nanoparticle's boundary layer, heating occurs. The nanowire dynamics is theoretically and experimentally investigated, and different feasibility proofs of the principle by physical modeling, which adhere to medical guidelines, are presented. The *magnetic nanorotors* exhibit rotations and oscillations with quite a steady center of gravity, which proves an immobile behavior and guarantees a time-independent homogeneity of the spatial particle distribution in the tumor. Furthermore, a fluid dynamic and thermodynamic heating model is briefly introduced. This model is a generalization of Penne's model that for this method reveals theoretic heating rates that are sufficiently high, and fits well into medical limits defined by present standards. *Published by AIP Publishing.* [<http://dx.doi.org/10.1063/1.4960406>]

### I. INTRODUCTION

Hyperthermia is a thermal cancer therapy, consisting of energy deposition into a malignant tumor. The associated temperature increase causes the subsequent destruction of cancer cells, while healthy cells, which are usually more robust, are spared. Depending on the steady state temperature in the tumor, hyperthermia can be classified as follows: (a) diathermy ( $T < 41^\circ\text{C}$ ), which is not desirable due to an acceleration of the tumor growth rate); (b) apoptosis ( $42^\circ\text{C} < T < 46^\circ\text{C}$ ), which describes a moderate hyperthermia; (c) thermoablation ( $T > 46^\circ\text{C}$ ), which causes heat-induced necrosis. Hyperthermia therapy can also be categorized in terms of the size of the targeted cancer region: (a) local; (b) regional, or (c) whole-body therapy. Thermal induction can be achieved by means of several external sources such as light, ultrasound, electromagnetic waves at the radiofrequency domain, or microwaves. Since Gilchrist *et al.*<sup>1</sup> proposed the concept of magnetically mediated hyperthermia, intensive research has been conducted in the development of effective thermoseeds for cancer therapies.

In magnetic hyperthermia methods, magnetic particles are injected into a cancer tumor, and tissue heating is initiated by an externally induced magnetic field effect, causing heat diffusion into the surrounding tumor cells. Magnetic particles used may have various shapes and sizes such as

nanospheres, elongated particles, crushed particles, octahedral prisms (see, e.g., Ref. 2), nanowires,<sup>3–5</sup> nanocrystals,<sup>5</sup> millimeter-sized nanocomposite spheres,<sup>2</sup> and needles (e.g., Refs. 6 and 7). The use of large-size thermoseeds requires the insertion of individual magnetic entities into the tumor (see, e.g., Refs. 6 and 7) and a subsequent resection after the hyperthermia treatment. Manipulation and internalization of very small entities is possible by means of colloidal systems such as ferrofluids (for example, see Ref. 8). In such methods, kinematic and physicochemical stability, influenced by magnetic, thermodynamic, and chemical effects is required. Sedimentation of larger particles by gravity forces must be considered. It is practically impossible to prepare stable suspensions containing particles with characteristic diameters larger than 20 nm.<sup>9</sup> If magnetic particles are injected intravenously into the target tissue, it is advantageous to replace the organic solvent of the ferrofluid by an aqueous solution.<sup>10</sup> Another internalization method uses hydrogels containing magnetic particles. In this case, the rheological fluid is directly incorporated into the tumor by injection (e.g., Ref. 11). Coating of the magnetic particles is often applied to prevent anisotropic magnetic dipolar attraction, for biocompatibility, for drug delivery, or to increase the thermal deposition energy. Iron oxide particles are the most widely investigated because of their biocompatibility and their ability to be metabolized.<sup>12</sup> After the insertion of magnetic particles into a cancer tumor, different heating mechanisms can be applied. Usually heating is generated by the application of a single frequency alternating or, in other

<sup>a)</sup>Author to whom correspondence should be addressed. Electronic mail: snaveen@ethz.ch

words, linearly polarized electric or magnetic field. Conventional heating methods include the Joule effect resulting from eddy currents, the bulk hysteresis effect, the dielectric effect, the Néel's and Brownian mechanisms,<sup>13,14</sup> and the magnetocaloric effect.<sup>15-17</sup>

Magnetic nano- and microscale particles may employ several of these effects simultaneously. The dominant heating mechanism will be determined as a function of the following: (a) the properties of the particles such as their geometry (i.e., spherical, ellipsoidal, and cylindrical), their composition or their magnetic behavior (i.e., superparamagnetism and ferromagnetism); (b) the properties of the fluid or the surrounding tissue environment such as its density and viscosity; and (c) the amplitude, frequency, and polarization of the magnetic field.

In sub- $\mu\text{m}$  particles, which exhibit a single magnetic domain, where bulk hysteresis effects by multiple domain wall motion and eddy current heating is negligible, there are in generality, *four heat generation mechanisms*. Stochastic thermal excitation is responsible for two of them while the other two are induced by a forcing of an externally applied magnetic field.

The first effect is *zero-field Néel relaxation*<sup>18</sup> where under a stochastic thermal excitation, the internal magnetic moment moves within the particle, flipping its state of magnetization in a double-well potential energy distribution,<sup>19</sup> in a dissipative manner, leading to an internal relaxation effect. The related relaxation time  $\tau_N$  is given by the following formula:<sup>13,18</sup>  $\tau_N = \tau_0 \exp[KV/(k_B T)]$ , where  $K$  denotes the anisotropy factor,  $V$  the volume of the nanoparticle,  $k_B$  the Boltzmann constant, and  $T$  the absolute temperature. The quantity  $\tau_0$  is called attempt time and is assumed to be of the order  $10^{-9}\text{s}$ .<sup>9</sup> The second thermal excitation effect is *Brownian relaxation*, where a particle physically executes a random rotational motion caused by a change of the direction of its net magnetic moment. Therefore, the relaxation time is composed by replacing in *zero-field Néel's relaxation* the magnetic anisotropy by the viscous dissipation physical term:  $\tau_N = \tau_0 \exp[3\eta V_H/(k_B T)]$ . In this formula,  $\eta$  denotes the dynamic viscosity of the fluid and  $V_H$  a hydrodynamic volume of the nanoparticle, which is slightly larger than the effective particle volume.<sup>13,20</sup> According to Dennis and Ivkov,<sup>21</sup> the time constant of this effect is of the order  $10^{-3}\text{s}$ , whereas Mamyia and Jeyadevan<sup>22</sup> report a value rather of the order of  $10^{-5}\text{s}$ .

In the case of external field forced nanoparticles, two additional effects come into play, namely, the *Néel forcing* which is the reversal of the internal magnetic moment under an external magnetic field,<sup>23-26</sup> and *Brownian forcing*, which is the physical rotation of a particle under the torque exerted by the external field.

We bring to the notice of readers that there exists potentially confusing and conflicting usage of the terminology of these two zero-field and two external-field mechanisms in literature. In previous works, the terms Néel and Brownian relaxation were used for the zero-field relaxations and simultaneously also for the external field driven effects. Whereas usage of these terms for thermally excited systems under zero field condition near equilibrium is appropriate,

for externally driven systems which are far from equilibrium, its usage is inaccurate<sup>25,27</sup> and even in contradiction to general physics terminology. This is the reason that we propose to replace *relaxation* by *forcing* in the latter two cases. Table I will assist the reader to the newly proposed terminology. We point out that more than one of the four effects may occur simultaneously, but to the best of our knowledge, no one has tackled the problem of a simultaneous modeling of such effects. However, in practice, usually a strong field driven effect dominates the weaker thermally induced effect.

The *Néel forcing* is generally considered to be of high heating efficiency. Thus in most magnetic hyperthermia applications, a high-frequency ( $\sim 10^5\text{Hz}$ ) alternating magnetic field (see, e.g., Refs. 28–30) is used, assuming mechanical immobilization of the particle, to utilize the *Néel forcing* as the dominant heating mechanism. The prospect of using a rotating or circularly polarized magnetic field rather than an alternating or linearly polarized field to drive the rotation of the internal magnetic moment in an immobilized nanoparticle was discussed recently by de Châtel *et al.*<sup>31</sup> They showed that the use of rotating fields does not exhibit an increased heating effect unless when operated at frequencies greater than  $10^8\text{Hz}$ .

It is important to note that a high magnetic field  $H_0$ , combined with a high frequency,  $f_M$ , can induce tissue damage by eddy current heating. The clinical limit of the product of these two physical quantities is generally agreed to be  $(H_0 * f_M)_{crit} < 5 \times 10^8 \text{A m}^{-1} \text{s}^{-1}$  (see, e.g., Refs. 32–36), a value which has been constantly confirmed in numerous *in vivo* experimental applications.

Modeling heat diffusion and perfusion in human tissues requires a deep understanding of the local environment and the relevant heat transfer processes. Seminal work of Pennes<sup>37</sup> considers an entire forearm, which is approximated by a cylindrical body. It is mainly a model designed on the basis of empirical observations. Major drawbacks of this model are the tissue homogeneity of such a large region and the simplification of the blood perfusion process (unidirectional, constant and no distinction of blood vessels with different sizes). The original Pennes's model consists of a single equation formulated in cylindrical coordinates with constant physical properties of the components of the human (e.g., skin, blood, muscle, etc.) and a constant metabolic heat source. Pennes's model has been widely recognized and

TABLE I. The newly proposed terminology for magnetic hyperthermia methods. It is proposed to distinguish the effects generated by thermal excitation and external magnetic field forcing. In the existing literature, the four physical methods of heat generation had only two names, namely, Néel and Brownian relaxation. Here, the external field driven effects are named Néel and Brownian forcing. The magnetic hyperthermia method presented in this article utilizes Brownian forcing.

Name of effect	Excitation/Forcing	Resistance	Equilibrium
Néel relaxation	Thermal excitation	Anisotropy effect	Close to eq.
Brownian relaxation	Thermal excitation	Fluid dissipation	Close to eq.
Néel forcing	External forcing	Anisotropy effect	Far from eq.
Brownian forcing	External forcing	Fluid dissipation	Far from eq.

applied, and several generalizations and improvements have been proposed, especially improving the description of the thermal effects of large vessels at the tissue domain. Because it is difficult to take into consideration the effect of each blood vessel with its particular heat exchange, Chen and Holmes introduced a statistical concept of the vessel size distribution. This work led to a generally accepted two-equation bio-heat model. Other models based on porous domains and the volume averaging method were developed by Wulf and Klinger. Further improvements led to three-equation models (models of Keller and Seiler, Chato, Raetzl and Xuan, Weinbaum and Jiji and Bejan) (for details of all these models see, e.g., Ref. 38). In these model refinements, the temperature distinction between the arteries and veins are taken into consideration. The small therapeutic temperature span required for an efficient hyperthermia treatment, that does not damage healthy cells, highlights the crucial need for high-quality thermal diffusion and perfusion modeling and simulation.

This article has four primary objectives. The first and main objective is to introduce the rotating nanowire hyperthermia method, which leads to heating induced by fluidic friction generated by active rotation of a magnetic nanowire driven by rotating magnetic fields. The second is to present the basic kinematic/dynamic theory and to validate it theoretically and experimentally. The third is to provide the main results of a fluid dynamic and thermodynamic model. Furthermore, the feasibility of the entire method is demonstrated by a theoretical-numerical study containing two specific application examples. In Sec. VII, an extensive parameter study reveals the good performance of the method and shows the influence of size and shape effects of a cancer tumor on dynamic behavior.

## II. KINEMATIC DESCRIPTION OF MOVING NANOWIRES

### A. The physical system

The proposed approach consists of injecting magnetic nanowires embedded in a highly viscous gel into the cancer tumor. The high-viscosity gel serves a two-fold purpose: (a) to fix the nanowires to the tumor site so that they do not penetrate into other healthy parts of the human body; (b) to guarantee that the friction between rotating nanowires and the gel generates heat (see Refs. 39–41). We note that these rotating nanowires can act as nanoscalpels if they are taken up or internalized by the cancer cells, and can destroy the cells by mechanical impact, a method recently proposed by Contreras *et al.*<sup>42</sup> Our study is not devoted to this alternate mechanism.

Magnetic torque cannot be induced in spherical superparamagnetic particles and gels,<sup>29</sup> because of their isotropic magnetic susceptibility. Therefore, our method applies to nanowires or other ferromagnetic particles,<sup>30</sup> which on account of their shape anisotropy and additionally by enhanced magneto-crystalline anisotropy by material design, can harbor a preferred magnetic easy axis. They obey the same rules as a compass needle in a magnetic field, albeit at smaller length scales.

The dynamics of a magnetic nanowire in a rotating magnetic field (Fig. 1) is governed by four different physical effects, which constitute the main differential equation. These are the *inertial torque*,  $\tau_I$ , of the nanowire, the *friction or resistance torque*,  $\tau_R$ , of the nanowire in the fluid, the *restoring magnetic torque*, which causes the nanowire to align parallel to the magnetic field lines, and the *forcing magnetic torque* of the nanowire. The magnetic torque contributions are combined into a single specific torque term,  $\tau_D$ . For the fluid friction torque, a small simple model has been developed, which has also been presented in Refs. 39 and 41. The thermal excitation term is ignored for the present analysis.

Following d'Alembert's principle, the equilibrium of all these torques gives us the main differential equation for the movement of a nanowire in a rotating magnetic field

$$\tau_I + \tau_R + \tau_D = 0. \quad (1)$$

Deriving and substituting the corresponding results for all torques (see Refs. 39, 41, and 43) lead to

$$\frac{\pi}{48} d^2 l^3 \rho_N \frac{d^2 \varphi_N}{dt^2} + \frac{5}{12} l^3 \rho_F \nu_F \frac{d \varphi_N}{dt} + \frac{\pi}{4} d^2 l \mu_0 H_0 M \sin(\varphi_N - \varphi_M) = 0. \quad (2)$$

A rearrangement of this equation yields

$$\frac{d^2 \varphi_N}{dt^2} + 2\rho \frac{d \varphi_N}{dt} + \omega_0^2 \sin(\varphi_N - \varphi_M) = 0, \quad (3)$$

with the following constant for the friction term:

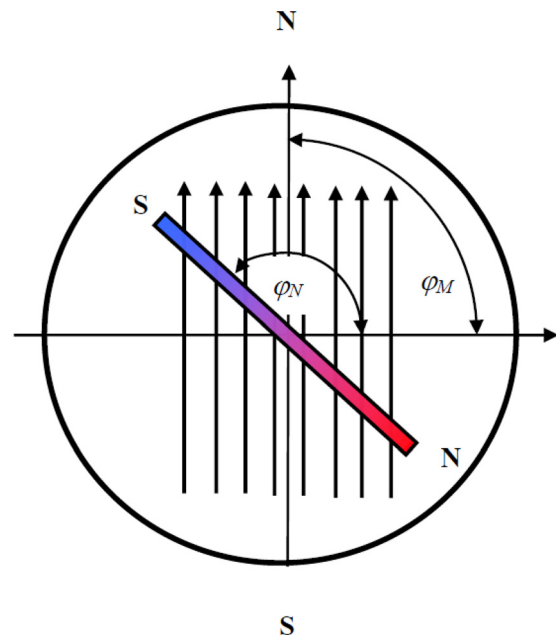


FIG. 1. A nanowire is forced to follow a rotating external magnetic field  $H_0 (\sin(\omega_M t), \cos(\omega_M t))$ . This situation leads to a nonlinear second-order ordinary differential equation, which is more general than the one of a forced harmonic oscillator with a frictional force proportional to the velocity of the body. This condition holds as long as the fluid motion is laminar, which is a realistic assumption for the proposed method with its small moving bodies.

$$\rho = \frac{10}{\pi} \frac{1}{d^2} \frac{\rho_F}{\rho_N} \nu_F, \quad (4)$$

and the constant for the term describing the coupling between the magnetic field and the nanowire, which is also identical to the eigen frequency of the nanowire

$$\omega_0 = \frac{2\sqrt{3}}{l} \sqrt{\frac{\mu_0 H_0 M}{\rho_N}}. \quad (5)$$

The rotation of magnetic nanowires in liquids has been studied in a general non-medical context by Keshoju *et al.*<sup>44</sup> Their theory corresponds well with the model presented in this article. These authors introduced the lag angle  $\varphi_L = \varphi_M - \varphi_N$ . However, there are only minor differences between the two modeling approaches such as the drag coefficient.

## B. Dimensional analysis

By making the differential equation (3) non-dimensional, we can write each variable by a characteristic value with a tilde symbol and a non-dimensional variable with a hat

$$\chi = \tilde{\chi} \hat{\chi}. \quad (6)$$

Then, the expression becomes

$$\frac{1}{\tilde{t}^2} \frac{d^2 \hat{\varphi}_N}{d\hat{t}^2} + \frac{2\rho}{\tilde{t}} \frac{d\hat{\varphi}_N}{d\hat{t}} + \omega_0^2 \sin(\hat{\varphi}_N - \hat{\varphi}_M) = 0, \quad (7)$$

where for constant quantities the tilde symbol is neglected. After multiplication by the characteristic time squared, one obtains

$$\frac{d^2 \hat{\varphi}_N}{d\hat{t}^2} + \Psi \frac{d\hat{\varphi}_N}{d\hat{t}} + \Omega \sin(\hat{\varphi}_N - \hat{\varphi}_M) = 0. \quad (8)$$

Adequate choices of the characteristic values are

$$\begin{aligned} \varphi_N &= \hat{\varphi}_N, & \varphi_M &= \hat{\varphi}_M, & \varphi_M &= \omega_M t = \frac{t}{\tilde{t}} = \hat{t} \\ \Rightarrow \tilde{t} &= \frac{1}{\omega_M} = \frac{T_M}{2\pi}. \end{aligned} \quad (9a-g)$$

The first dimensionless quantity is

$$\Psi = 2\rho \tilde{t} = \frac{20}{\pi} \frac{1}{d^2} \frac{\rho_F}{\rho_N} \frac{\nu_F}{\omega_M}, \quad (10a,b)$$

which describes the ratio of fluid friction force to the inertial force. The second dimensionless quantity is

$$\Omega = \omega_0^2 \tilde{t}^2 = 12 \frac{\mu_0 H_0 M}{l^2 \rho_N \omega_M^2}, \quad (11a,b)$$

which describes the ratio of restoring magnetic force to the inertial force.

## C. A three-dimensional coupled evolution differential equation

Now we rewrite the variables in the following manner (see Ref. 41):

$$x = \hat{\varphi}_N, \quad y = \frac{d\hat{\varphi}_N}{d\hat{t}}, \quad z = \hat{t}. \quad (12a-c)$$

With these new variables, the following system of three first-order differential equations is derived, which are also called the evolution equations of the nanowire:

$$\left| \begin{aligned} \frac{dx}{d\hat{t}} &= y \\ \frac{dy}{d\hat{t}} &= -\Psi y - \Omega \sin(x - z) \\ \frac{dz}{d\hat{t}} &= 1 \end{aligned} \right|, \quad (13a-c)$$

and where for simplicity we have set  $t = \hat{t}$ . The variable  $z$  describes the driving term by a linear increase of the angle of the magnetic field as function of time  $t$ . To solve this system of three ordinary differential equations, a simple first-order forward Euler algorithm is applied.

## D. The theoretical solutions of practical relevance

The solutions of the system of evolution equations (13a)–(13c) vary with the two dimensionless parameters  $\Psi$  and  $\Omega$ . In the framework of nonlinear dynamics, the variety of different types of movements is rich; however, we only discuss the two cases, which are of practical relevance

$$(1) \quad \Psi \gg 1 \quad \text{and} \quad \Psi \gg \Omega. \quad (14a,b)$$

In this strong viscous case, it follows from Equations (13a) and (13b)

$$y = 0 \Rightarrow x(t) = x(0) = 0 \quad (15a-c)$$

that the angular velocity is zero. It is assumed that the initial angle at  $t=0$  is also zero (see Eq. (15c)). Therefore, as expected, the result is no net movement of the nanowire. A numerical result of this simple solution is shown in Fig. 2. This is the case that should be avoided for hyperthermia applications, as it does not lead to heating by fluid friction.

$$(2) \quad \Omega \gg 1 \quad \text{and} \quad \Omega \gg \Psi. \quad (16a,b)$$

The preferred movement for hyperthermia is a strong coupling between the rotation of the magnetic field and the nanowire with only a minor phase shift between them. In general, the phase shift depends on the magnetic field strength and frequency, the particle dimensions, and the viscosity of the fluid (compare with figure caption and graphics of Fig. 3). If  $\Omega$  is larger than  $\Psi$  and 1, it follows that

$$\begin{aligned} \sin(x - z) = 0 &\Rightarrow x - z \in \pi \cdot n, \\ n &\in \{\dots - 2, -1, 0, +1, +2, \dots\}. \end{aligned} \quad (17a,b)$$

With  $n=0$ , one observes

$$x - z = 0 \quad \Rightarrow \quad x = z(t) \quad (18a,b)$$

that the nanowire strictly follows the movement of the magnetic field. A numerical simulation of this case is shown in Fig. 3. The damping was not chosen to be so strong that the

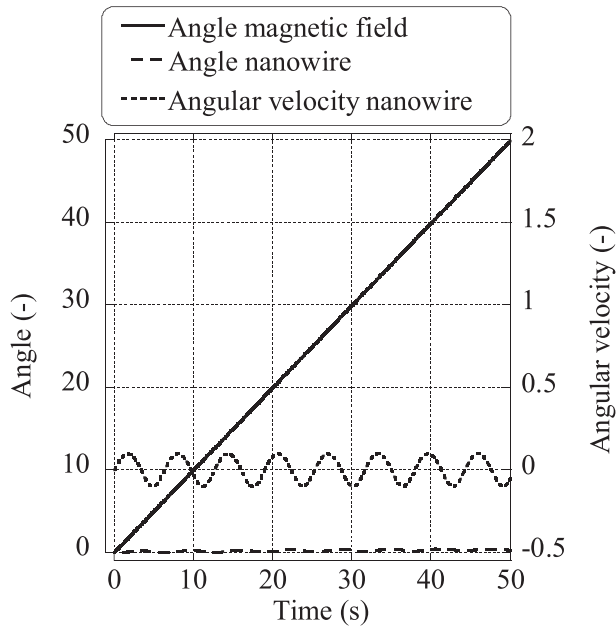


FIG. 2. The high-viscosity solution where the tumor tissue with injected fluid is too viscous to allow movement of a nanowire ( $\Psi = 100$ ,  $\Omega = 10$ ,  $\Delta t = 0.01$ , and  $x_0 = y_0 = z_0 = 0$ ) is shown. The magnetic field rotates with a constant angular velocity ( $\text{s}^{-1}$ ). This leads to a linear increase of its rotation angle (solid line). The rotation angle of the nanowire remains essentially constant (interrupted line), though it actually oscillates with a very small amplitude around the angle zero. This can be seen in the angular velocity of the nanowire, a signal that reveals the small oscillation (dotted line).

oscillation of the nanowire around the oscillating magnetic field completely vanishes at the beginning of the moving process.

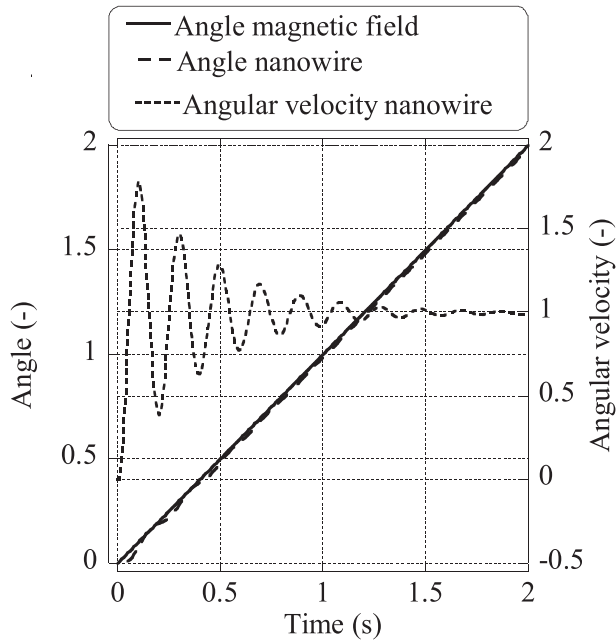


FIG. 3. In this case, the viscosity is smaller so that the nanowire can follow the magnetic field rotation ( $\Psi = 15$ ,  $\Omega = 1000$ ,  $\Delta t = 0.01$ , and  $x_0 = y_0 = z_0 = 0$ ). One can see the perfect straight (solid) line of the magnetic field movement and the initially small oscillation of the nanowire around the magnetic field line (dotted line). This oscillation can be better observed by looking at the angular velocity ( $\text{s}^{-1}$ ). The nanowire fulfills a damped motion and after circa 1.5 s is perfectly aligned with the magnetic field. A small phase shift to the back (lee side) is detected that shows that the nanowire is pulled by the magnetic field.

From inequality (16b), it follows that

$$\frac{5}{3\pi} \left(\frac{l}{d}\right)^2 \frac{\rho_F \nu_F \Omega M}{\mu_0 H_0 M} \ll 1, \quad (19)$$

and one finds the necessary critical external magnetic field  $H_{0,crit}^*$ , which must be overcome to guarantee a rotation of the nanowires

$$H_{0,crit}^* = \frac{5}{3\pi} \left(\frac{l}{d}\right)^2 \frac{\rho_F \nu_F \Omega M}{\mu_0 M}. \quad (20)$$

It becomes clear that a strong magnetic field and magnetization, a small density of the carrier fluid/tissue mixture and a small angular velocity permits a higher viscosity of the carrier fluid and human tissue mixture. If the magnetization is induced by the magnetic field, e.g., by a linear relation with the susceptibility as coefficient of proportionality, it follows that

$$M = \chi H_0 \Rightarrow H_{0,crit}^* = \sqrt{\frac{5}{3\pi}} \sqrt{\frac{\rho_F \nu_F \Omega M}{\mu_0 \chi}} \left(\frac{l}{d}\right). \quad (21)$$

The nanoparticles are assumed to float in the bulk of the gel. In case of floating on a gel surface, the theory requires a generalization with the surface tension effect. A similar formulation has been published by Yang *et al.*,<sup>20</sup> also leading to a critical field value, which up to a constant (in the case of Yang's theory including an aspect ratio of the nanowire) is identical. Up to this critical field-frequency combination, the particle physically rotates synchronously with the applied rotating magnetic field. Keeping the field amplitude constant and increasing the frequency, the particle cannot synchronously follow the applied field as the viscous torque on the nanowire increases, while the magnetic torque stays the same. Increasing the frequency further almost immobilizes the wire. This is a regime where *Néel forcing* under circularly polarized magnetic fields occurs and which has been recently investigated and reported to be less efficient than linear polarized field operation.<sup>31</sup> Our methodology operates at or below the critical field-frequency limit, where there is physical rotation of the particle under the external magnetic field (*Brownian forcing*), and the magnetization direction does not change internally within the particle.

At these spatial scales, a linear susceptibility model (Eq. (21)) works only for paramagnets and superparamagnets. For ferromagnets, it is more appropriate to apply Eq. (20) and to substitute  $M = M_r = 0.8, \dots, 1.0 M_s$ , where  $M_r$  denotes the remanence magnetization and  $M_s$  the saturation magnetization ( $M_s$ , e.g., of FeCo: 2.35 T, Ni: 0.62 T, and Fe: 2.15 T). Because of a high aspect ratio and a tailored magnetocrystalline anisotropy, nanowires may show bistable magnetic behavior (see also Ref. 45).

The set of differential equations contains a richer variety of motion than just the one of practical importance given by Eq. (18b). A thorough discussion of all the different moving modes will be presented later. Furthermore, the near equivalence of equations (13a)–(13c) to those of a periodically kicked oscillator raises the question if chaotic motion occurs and if in the phase diagram  $\Psi(\Omega)$  the existence of (fractal) Arnold tongues will be observed (see Ref. 41) as has been



FIG. 4. The experimental set-up: The four electromagnets produce a homogeneous magnetic field in the workspace. The electromagnet consists of a soft-magnetic FeCo core (the diameter is 13.5 mm and the length 30 mm) wound with 0.7 mm diameter copper wire to a total outer diameter of 53.5 mm. For image capture a 20× Mitutoyo objective lens (NA = 0.52) is coupled to a high-speed camera (BASLER acA2000).

found in the corresponding phase space of a nonlinear pendulum with periodic Dirac pulse forcing (see, e.g., Ref. 46) and in nonlinear electrochemical oscillators by Nakato *et al.*<sup>47</sup>

### III. EXPERIMENTS

#### A. The experimental set-up

The experimental set-up consists of four in-planar and orthogonally mounted electromagnets (Fig. 4). Two opposing coils are driven with a sinusoidal current signal, and the other pair of coils receives a  $\pi/2$ -phase shifted current signal of equal amplitude. This produces a rotating magnetic field. In this system, the amplitude of the magnetic field can be varied from 0 to 30 mT. Between the four magnetic coils, there is a sample holder for the nanowire-fluid suspension. A high-speed camera attached to a 20× objective lens captures the dynamics of nanowire motion.

#### B. First experimental observations

In the first experiments, rotational and oscillatory modes depending on the frequency of the magnetic field rotation were recorded (see Fig. 5). The external magnetic field strength in the experiments was 7 mT, and the frequency of magnetic field rotation was varied from  $f_M = 1$  Hz up to 30 Hz. Nickel nanowires (with a saturation magnetization  $M_s = 0.62$  T) were produced in the Micro- and Nanotechnology (MNT) laboratory of the UASW. Their production is described in detail in Refs. 40 and 41. The nanowire's mean diameter was  $d = 200$  nm, and their length was  $l = 5$   $\mu\text{m}$ . The density of the nanowires was  $\rho_N = 7870$   $\text{kg m}^{-3}$ . The used glycerol gel has a density of  $\rho_F = 1400$   $\text{kg m}^{-3}$  and a kinematic viscosity of  $\nu_F = 1.180 \times 10^{-3}$   $\text{m}^2 \text{s}^{-1}$ .

It is observed that the nanowires approximately spin around their centers of gravity with minor translational movements of these center points. The absence of detectable translational movement is necessary to guarantee a good spatial homogeneity of the nanowires. Zhang *et al.*<sup>48</sup> observed propulsion and cargo transport of rotating nickel nanowires located close to patterned surfaces. The practical

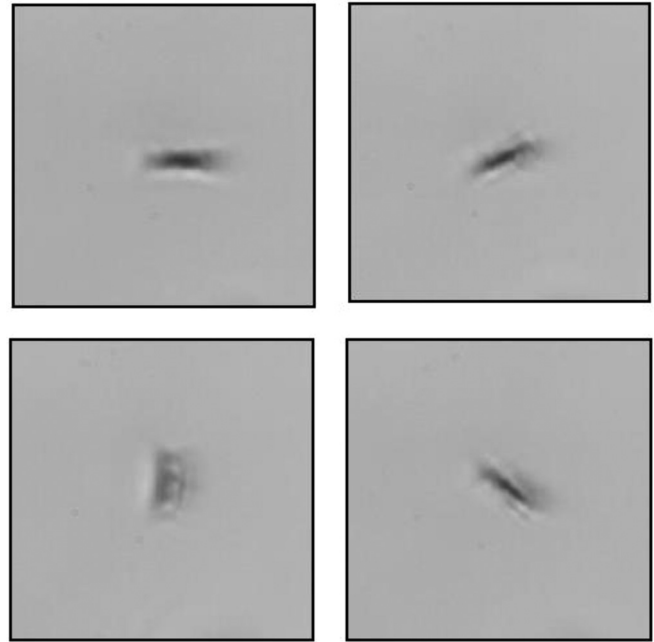


FIG. 5. Images of a rotating nickel nanowire of length 5  $\mu\text{m}$  and a diameter of 200 nm, suspended in glycerol gel and driven by a planar rotating magnetic field, are presented. The nanowire performs a continuous smooth rotation of 10 Hz in anti-clockwise direction. Visually, no mobility of the center of gravity is observed, a fact that favors good homogeneity of the particle distribution in the carrier fluid.

hyperthermia application may require slightly other parameters than the ones introduced in Sections II and III. In Section V, a feasibility study demonstrates the applicability of this method for realistic (characteristic) parameters and shows that for rotating nanowires sufficient heating rates are to be expected.

### IV. FLUID AND THERMODYNAMIC MODELING

#### A. Geometrical description of the tumor

In this work, tumor regions are approximated as spheroids, which are ellipsoids with two identical half axis  $a = b$  and a usually differing third half axis  $c$  (see Fig. 6). The surface area of a tumor is given by the following equation (see Refs. 33 and 37):

$$A_{\text{spheroid}}(m, n) = 2\pi a^2 [1 + G_\chi(m, n)],$$

$$\left. \begin{array}{l} a > c : \chi = \text{oblate} \\ a = c : \chi = \text{spherical} \\ a < c : \chi = \text{prolate} \end{array} \right\} \begin{array}{l} m = \min\{a, c\} \\ n = \max\{a, c\}, \end{array} \quad (22a-c)$$

with the definition of the ellipticity of the spheroid formed by the cross section through its center

$$e(\xi, \psi) = \sqrt{1 - \frac{\xi^2}{\psi^2}}. \quad (23)$$

The three different partial functions of the spheroid's surfaces are directly related to the geometrical factor  $g$ , which is defined in Eq. (27e) and presented in Fig. 7. They are

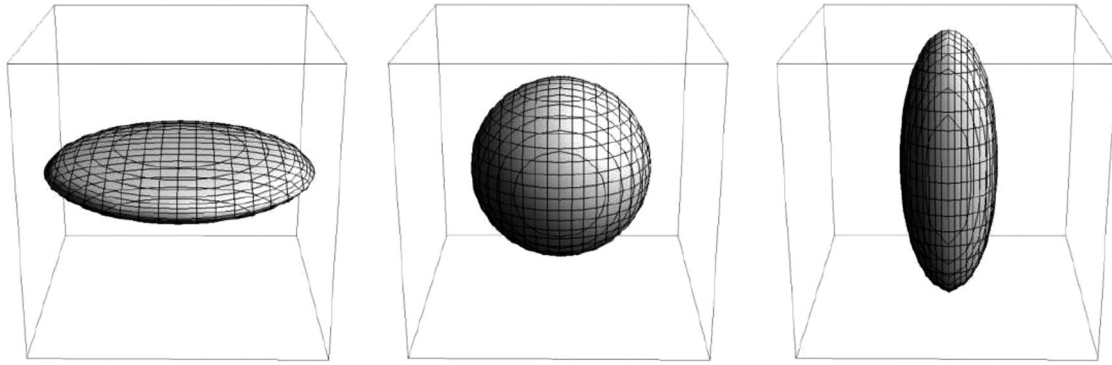


FIG. 6. Spheroids can approximate many possible occurring tumors, as, for example, (a) flat objects (as occurring in skin cancer), (b) spherical tumors as they occur more inside the human body, and also (c) deep ranging finger-like objects, preferentially also located in the interior of the body (from Refs. 39 and 43).

$$G_{oblate}(m, n) = \frac{1 - e^2(m, n)}{e(m, n)} \text{area}$$

$$\tanh[e(m, n)] = \frac{1 - e^2(m, n)}{2e(m, n)} \log_e \left[ \frac{1 + e(m, n)}{1 - e(m, n)} \right],$$

$$G_{spherical}(m, n) = 1,$$

$$G_{prolate}(m, n) = \frac{1}{e(m, n) \sqrt{1 - e^2(m, n)}} \arcsin[e(m, n)]. \quad (24a-d)$$

The volume of a spheroid is

$$V = \frac{4\pi}{3} a^2 c. \quad (25)$$

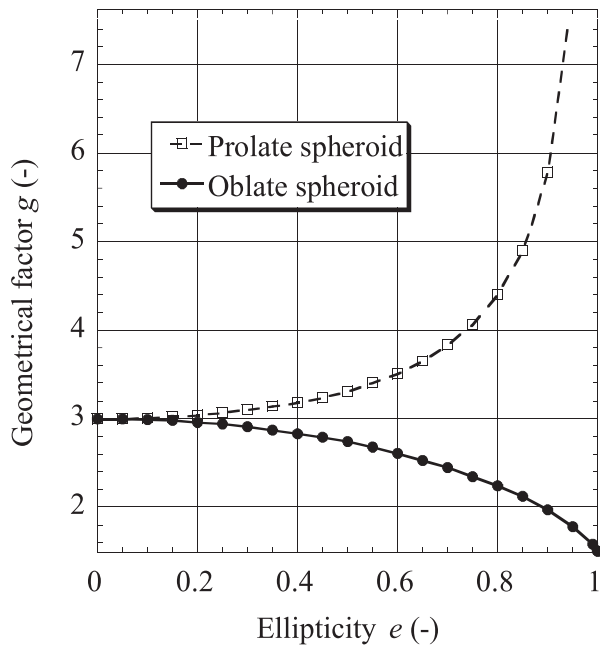


FIG. 7. The main geometrical factor  $g = 3/2(1 + G_g)$  (see also Eq. (27e)) is presented as a function of the ellipticity  $e(m, n)$ . Ellipticity zero corresponds to the geometrical factor  $g = 3$  and describes a spherical tumor. Prolate spheroids exhibit higher  $g$  factors than oblate ones. An ellipticity of one corresponds to a  $g$  factor of  $3/2$  in the oblate case and approaches infinity in the prolate case. It is to be noted that the  $g$  factor, and by this a geometrical dependence, only occurs in the time constant of diffusion (compare with Pennes number,  $Pn$ , see Section IV F).

## B. Fluid dynamic and thermodynamic model

A simplified thermodynamic model, presented in Refs. 39, 41, and 43 in more detail, is applied to the presented hyperthermia method. It assumes a homogeneous temperature distribution in the tumor (Fig. 8). Energy conservation with the approximation ( $m_T c_{pT} \gg m_P c_{pP}$ ) states that

$$\frac{dQ_T}{dt} = \dot{Q}_D + \dot{Q}_B + \dot{Q}_M + \dot{Q}_P,$$

$$\frac{dT_T}{dt} = \frac{1}{m_T c_{pT}} (\dot{Q}_D + \dot{Q}_B + \dot{Q}_M + \dot{Q}_P), \quad (26a, b)$$

where the index  $D$  denotes diffusion,  $B$  blood perfusion (convective transport by the blood flow),  $M$  the metabolic heat

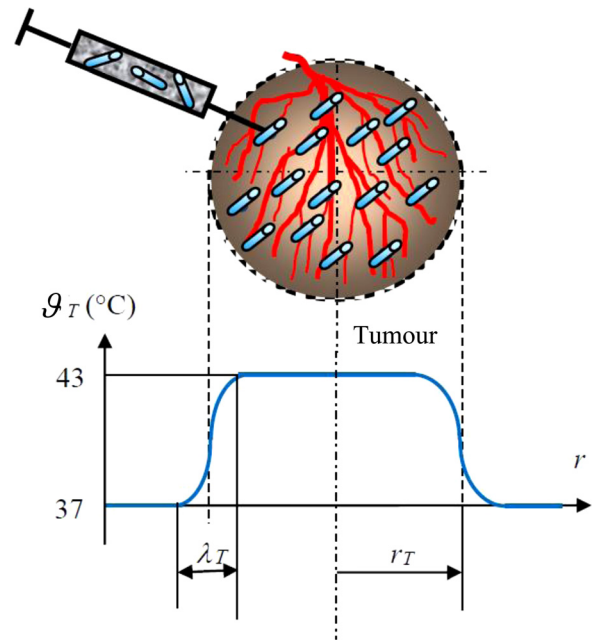


FIG. 8. A spherical tumor with veins and arteries of radius  $r_T$  and its heating by magnetic nanowires from, e.g.,  $37^\circ\text{C}$  to  $43^\circ\text{C}$  is shown. At the border of the cancer tumor, by heat losses given by heat diffusion, the temperature profile decreases over the diffusion length  $\lambda_T$ . The red lines show arteries and veins with a blood mass flow and heat transport by fluid convection. Heat sources are defined by the metabolic heat production, but mainly by the application of one of the existing hyperthermia heating methods (the figure is from Ref. 39).

production source term, and  $P$  the applied heating method. This model in its general derivation is valid for any kind of heat source term. By specifying a source and by modeling it, a special tailored model for the chosen hyperthermia method is obtained, in our case for rotating nanowires with fluid friction.

The final result is given by five equations, one for the temperature distribution  $T_T(t)$ , one for the steady state temperature  $T_\infty$ , which is the temperature that occurs after some transition time, the specific heat source term  $\dot{q}$ , the time constant  $\tau$  of the process, and the definition of the geometric parameter  $g$

$$\begin{aligned} T_T(t) &= T_E + (T_\infty - T_E) \left\{ 1 - \exp\left[-\frac{t}{\tau}\right] \right\}, \\ T_\infty - T_E &= \frac{\dot{q}\tau}{\rho_T c_{pT}}, \quad \dot{q} = \dot{q}_M + c\dot{q}_{P,Mat}, \\ \tau &= \frac{1}{\left\{ \frac{g\alpha_T}{c_T \lambda_T} + \frac{c_{PB}\omega}{\rho_T c_{pT}} \right\}}, \quad g = \frac{3}{2} [1 + G_\chi(m, n)]. \end{aligned} \quad (27a-e)$$

### C. The characteristic diffusion length

The physical model presented so far is clearly defined, with one exception, the diffusion length  $\lambda_T$ . This free parameter has the character of an empirical constant and originates in the approximate character of the model. For an improvement, the model requires a full description in elliptical coordinates. In the cases presented in this article, practically the same results, as derived by the simpler model considerations in this section, would be obtained.

With Eqs. (35), (36a), and (36b) and the Fourier criterion  $Fo = 1$  (see in Table III, last column), a cubic, respectively, quadratic equation results that can be solved and leads to

$$\lambda_T = \frac{1}{2} \frac{gk_T}{c_{PB}\omega c_T} \left( \sqrt{1 + 4 \frac{c_{PB}\omega c_T^2}{g^2 k_T}} - 1 \right). \quad (28)$$

It is clear that a vanishing thermal conductivity leads to a diffusion length of zero.

### D. The source term of the hyperthermia method

The basis to calculate heating by fluid friction is the resistance term in the kinematical equation (13b).

A basic physical equation states that

$$\dot{Q}_{P,Mat} = \tau_R \omega_N. \quad (29)$$

The torque of fluid friction is (see Ref. 41)

$$\dot{Q}_{P,Mat} = \frac{5}{12} l^3 \rho_F \nu_F \left( \frac{d\varphi_N}{dt} \right)^2 = \frac{5}{12} l^3 \rho_F \nu_F \omega_N^2, \quad (30a,b)$$

where the sign was changed to have a positive heat input by fluid friction. Now a movement where the needle exactly follows the magnetic field rotation is considered

$$\omega_N = \omega_M. \quad (31)$$

This leads to the final result for the volumetric specific heat source term of the magnetic material

$$\dot{q}_{P,Mat} = \frac{5}{12} \frac{l^3 \rho_T \nu_T \omega_M^2}{V_p} = \frac{5}{3\pi} \left( \frac{l}{d} \right)^2 \rho_T \nu_T \omega_M^2, \quad (32a,b)$$

where  $V_p$  denotes the volume of a particle, which in our case is a cylindrical nanowire. Furthermore, the index  $F$  (fluid) was changed to  $T$  (tumor). The idea realized is that the heat produced by fluid friction in a nanowires boundary layer is fictitiously and homogeneously distributed over the nanowire's entire domain to lead to a usual specific heat source term of the rotating nanowires.

### E. The final model formulation

An additional modification is performed to obtain the final model formulation. The intention is to describe the heat source term, describing the particle heating, by introducing Eq. (32b). By this, the model loses its generality in the sense that it no longer applies to all hyperthermia methods, but instead represents the *specific model* for the rotating nanowire hyperthermia method. The final kinematic, fluid-dynamic and thermodynamic model formulation is the following:

$$\begin{aligned} T_T(t) &= T_E + (T_\infty - T_E) \left[ 1 - \exp\left(-\frac{t}{\tau}\right) \right], \\ T_\infty - T_E &= \frac{\dot{q}\tau}{\rho_T c_{pT}}, \\ \dot{q} &= \dot{q}_M + \frac{5}{3\pi} \left( \frac{l}{d} \right)^2 c_{pT} \nu_T \omega_M^2, \\ \tau &= \frac{1}{\left\{ \frac{g\alpha_T}{c_T \lambda_T} + \frac{c_{PB}\omega}{\rho_T c_{pT}} \right\}}, \\ g &= \frac{3}{2} [1 + G_\chi(m, n)], \\ \lambda_T &= \frac{1}{2} \frac{gk_T}{c_{PB}\omega c_T} \left( \sqrt{1 + 4 \frac{c_{PB}\omega c_T^2}{g^2 k_T}} - 1 \right). \end{aligned} \quad (33a-f)$$

The heating up of a tumor is described by an exponential function independent of its geometry (oblate spheroid, spheroid, or prolate spheroid). One also sees in Eqs. (33b) and (33c) that a higher heating rate leads to a higher final temperature of the tumor, whereas a high thermal capacity has the opposite effect. The time constant  $\tau$  is influenced by practically all occurring parameters, so it results, for example, that a high perfusion rate leads to a smaller time constant of the heating process.

## F. Dimensional analysis

To describe the problem dimensionlessly, four dimensionless numbers are introduced

### (1) Pennes number, Pn:

The Pennes number is defined by the ratio of two time constants

$$Pn = \frac{\tau_D}{\tau_B}. \quad (34)$$

For combinations of time constants, the following law is valid:

$$\tau = \frac{1}{\frac{1}{\tau_D} + \frac{1}{\tau_B}}. \quad (35)$$

A comparison of Eq. (35) with (27d), the time constants for diffusion,  $\tau_D$ , and blood perfusion,  $\tau_B$ , are determined to be

$$\tau_D = \frac{c_T \lambda_T}{g \alpha_T}, \quad \tau_B = \frac{\rho_T c_{pT}}{c_{pB} \omega}. \quad (36a,b)$$

Now Pennes's number is obtained by substituting Eqs. (36a) and (36b) into (34)

$$Pn = \frac{c_T \lambda_T c_{pB} \omega}{g \rho_T c_{pT} \alpha_T} = \frac{c_T \lambda_T c_{pB} \omega}{g k_T}, \quad (37a,b)$$

where also (28) and

$$\alpha_T = \frac{k_T}{\rho_T c_{pT}}, \quad (38)$$

were applied.

### (2) Tishin number, Ti:

The Tishin number is defined by the ratio of two other time constants

$$Ti = \frac{\tau_D}{\tau_M}. \quad (39)$$

By substituting Eq. (36a) into (39) and applying again some previous equations, it follows:

$$Ti = \frac{c_T \lambda_T}{g \alpha_T \tau_M} = \frac{c_T \lambda_T \rho_T c_{pT} \omega_M}{g k_T}, \quad \tau_M = \frac{1}{\omega_M}. \quad (40a-c)$$

### (3) Rosensweig number, Rs:

The Rosensweig number is defined by

$$Rs = \frac{T_\infty}{T_E} - 1. \quad (41)$$

By comparison with Eq. (33b), divided by  $T_E$ , it also follows that

$$Rs = \frac{\dot{q}\tau}{\rho_T c_{pT} T_E}. \quad (42)$$

### (4) The Croci number, Cr:

The Croci number is defined as the ratio of heat produced by the nanoparticles, respectively, nanowires, to the one produced by metabolism

$$Cr = \frac{\dot{Q}_P}{\dot{Q}_M}. \quad (43)$$

From Eqs. (33c) and (41), one concludes that

$$Cr = \frac{\dot{q}_P}{\dot{q}_M} = \frac{5}{3\pi} \left(\frac{l}{d}\right)^2 \frac{c \rho_T \nu_T \omega_M^2}{\dot{q}_M}. \quad (44a,b)$$

Now two dimensionless variables are introduced

$$\tilde{t} = \frac{t}{\tau_M}, \quad \theta_T = \frac{T_T - T_E}{T_E}. \quad (45a,b)$$

Then, it follows from (33a) with (37a), (40a), and (41)

$$\theta_T = Rs(Cr) \left[ 1 - \exp\left(-\frac{1 + Pn}{Ti} \tilde{t}\right) \right]. \quad (46)$$

## G. Additional model results

To present the model results in a concise manner, we introduce another dimensionless temperature

$$\hat{T}_T = \frac{T_\infty - T_T}{T_E}, \quad (47)$$

and rewrite Eq. (46), with help of Eqs. (41), (45b), and (48c) (see next line), to become

$$\begin{aligned} \hat{T}_T &= Rs \cdot \exp\left(-\frac{1 + Pn}{Ti} \hat{t}\right), \\ \hat{T}_T &= Rs \cdot \exp\left(-\frac{1 + Pn}{Ti} \frac{\tau_1}{\tau_F} \tilde{t}\right), \quad \tilde{t} = \frac{t}{\tau_1}, \end{aligned} \quad (48a-c)$$

with  $\tau_1 = 1$  h (hour). Taking the natural logarithm of this equation leads to a linear equation

$$\log_e \hat{T}_T = -\frac{1 + Pn}{Ti} \frac{\tau_1}{\tau_F} \tilde{t} + \log_e Rs. \quad (49)$$

In hyperthermia treatments, the temperature range of all applied methods is rather limited, and by this, the Rosensweig number,  $Rs$ , does not vary over a very large domain. A corresponding graphics of the final results, calculated by applying Eq. (49), is shown in Fig. 9.

A Taylor expansion of the exponential function in Eq. (48a) for small values of its argument leads to

$$\begin{aligned} \exp\left(-\frac{1 + Pn}{Ti} \hat{t}\right) &= 1 - \frac{1 + Pn}{Ti} \hat{t} + O\left[\left(\frac{1 + Pn}{Ti} \hat{t}\right)^2\right], \\ \hat{t} &\ll \frac{Ti}{1 + Pn}. \end{aligned} \quad (50a,b)$$

This result is substituted into Eq. (48a) to obtain another linear dependence

$$\hat{T}_T = Rs \left[ 1 - (1 + Pn) \frac{Rs}{Ti} \hat{t} \right]. \quad (51)$$

This linear function is useful for the study of the initial phase of the heating process.

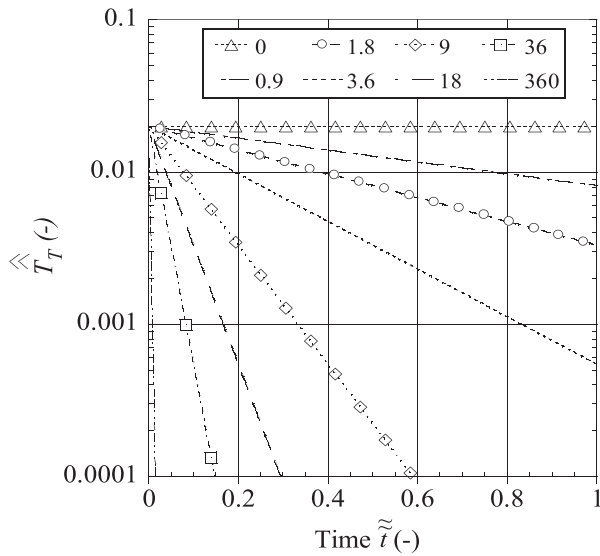


FIG. 9. The dimensionless temperature, given in Eq. (48b), is shown as a function of the time normalized with one hour for the first parameter being  $R_S = 0.02$ . This value corresponds to a blood temperature of  $37.0^\circ\text{C}$  and a final heated tumor temperature of  $43.2^\circ\text{C}$ . The second parameter listed is an inverse time, namely,  $(1 + Pn)/Ti_s(\tau_1/\tau_F)$ , with  $\tau_1 = 1$  h, which varies between the values 0 and 360. For this case, useful parameters to obtain characteristic heating times substantially less than half an hour can be easily found.

## V. FEASIBILITY OF PRACTICAL APPLICATION

We used the magnetic field generator, presented in detail in Section III, to run preliminary experiments to corroborate the model predictions.

The nanowires used in the experiments showed slightly larger dimensions ( $d = 200$  nm and  $l = 5000$  nm) than those required for a practical hyperthermia application. This was done to ensure visibility of nanowire motion by optical means. The further parameters are those given in the first paragraph of Section III B. If these parameters are inserted into Eq. (20), it follows that our theory predicts a critical

magnetic field of  $H_{0,crit}^* = 7$  mT for a drive frequency of  $f_M = 1$  Hz for nanowires in 65%–35% glycerol-water mixture. Experimentally, we observe that the wire starts to turn at approximately  $H_0 = 5$  mT. At  $H_0 = 7$  mT and  $f_M = 30$  Hz, the nanowire does not rotate and roughly oscillates around its geometrical center (the theoretical prediction by Eq. (20)) is  $H_{0,crit}^*$  is 210 mT. Therefore, our model not only predicts the theoretically expected movements but also yields very good threshold values for the rotational movement.

To prove the practical feasibility of the presented hyperthermia method, we used nanowire model geometries which are of dimensions one order smaller than those used in the experiments above. We demonstrate two sets of practically viable magnetic field-frequency combinations that meet the medical and clinical safety guidelines (see Section VI) and their corresponding nanowire geometry and concentration. The requirement of the optimal parameter set was to obtain a heating of a spherical tumor (radius 30 mm) to the final temperature of  $43^\circ\text{C}$ . The parameters of the two examples (FS1 and FS) of the feasibility study are presented in Tables II–IV in lightface and bold, respectively. All the dimensionless numbers are listed in Table III, and the calculation results of the two proposed cases are listed in Table IV.

It is possible to find a parameter set for which hyperthermia with rotating nanowires and fluid friction will work successfully. Our numerical calculations show that with increasing frequency this hyperthermia method shows a large increase in heating power. Therefore, reaching large heating rates—even with small particle concentrations—is feasible and makes this method highly attractive for further development. To apply the model, the continuum limit of fluid dynamics must be fulfilled, by adjusting parameters that lead to a low Knudsen number. Because of the small geometrical dimensions of the nanowires, the Reynolds numbers are extremely small (see Table III) such that laminar flow is guaranteed around the rotating nanowires.

TABLE II. The input parameters (characteristic values) for the model calculations are grouped into external parameters, nanowire data, and tumor data and are systematically listed in this table.

External parameters	Symbol	Num. value FS1/FS2	Unit
Frequency	$f_M$	$5.000 \times 10^3 / \mathbf{1.000} \times \mathbf{10^3}$	Hz
Temperature human body	$T_E$	$3.700 \times 10^1$	$^\circ\text{C}$
<i>Data nanowire</i>			
Concentration	$c$	$2.260 \times 10^{-5} / \mathbf{9.040} \times \mathbf{10^{-5}}$	$(\text{m}^3 \text{m}^{-3})$
Diameter of nanowire	$d$	$5.000 \times 10^1 / \mathbf{1.000} \times \mathbf{10^1}$	nm
Length of nanowire	$l$	$1.000 \times 10^2 / \mathbf{5.000} \times \mathbf{10^1}$	nm
Magn. Perm. of vacuum	$\mu_0$	$1.257 \times 10^{-6}$	$\text{N A}^{-2}$
Magnetisation (FeCo nanow.)	$M$	$1.8700 \times 10^6$	$\text{A m}^{-1}$
<i>Data tumor</i>			
Geom. parameter of tumor	$g$	$3.000 \times 10^0$	...
Radius of tumor	$c_T = r_T$	$3.000 \times 10^{-2}$	m
Density of tumor	$\rho_T$	$1.100 \times 10^3$	$\text{kg m}^{-3}$ , Ref. 49
Spec. heat capacity of tumor	$c_{pT}$	$4.200 \times 10^3$	$\text{J kg}^{-1} \text{K}^{-1}$ , Ref. 49
Therm. conductivity of tumor	$k_T$	$5.500 \times 10^{-1}$	$\text{W m}^{-1} \text{K}^{-1}$ , Ref. 49
Kin. viscosity of tumor	$\nu_T$	$1.180 \times 10^{-3}$	$\text{m}^2 \text{s}^{-1}$ , Ref. 49
Diffusivity of tumor	$\alpha_T$	$1.190 \times 10^{-7}$	$\text{m}^2 \text{s}^{-1}$
Spec. heat cap. of blood	$c_{pB}$	$3.770 \times 10^3$	$\text{J kg}^{-1} \text{K}^{-1}$ , Ref. 49
Blood perfusion rate	$\omega$	$7.550 \times 10^{-1}$	$\text{kg m}^{-3} \text{s}^{-1}$ , Ref. 49

TABLE III. Six dimensionless numbers are listed. Four of them are newly proposed definitions related to magnetism and nanotechnology. The last two are the well-known Fourier and Reynolds number, named after Jean Baptiste Joseph Fourier and Osborne Reynolds.

Number	Abbreviation	Numerical value	Source of calculation
Pennes number	$Pn$	$3.761 \times 10^{-1}$	Eq. (34)
Tishin number	$Ti$	$1.918 \times 10^7/3.835 \times 10^6$	Eqs. (39) and (40a)
Rosensweig number	$Rs$	$1.622 \times 10^{-1}$	Eqs. (41) and (42)
Croci number	$Cr$	$5.818 \times 10^1$	Eqs. (43) and (44b)
Reynolds number	$Re$	$6.656 \times 10^{-8}/3.328 \times 10^{-9}$	$Re = \omega_M l^2 / (4\nu)$
Fourier number	$Fo$	$1.000 \times 10^0$	$Fo = \alpha_T \tau / (\lambda_T)^2$

TABLE IV. Calculated results performed with the model equations of this article are listed. Some applied equations are shown in the last column.

Phys. Quantity	Symbol	Numerical value	Unit	Source
Volume of nanowire	$V_P$	$1.964 \times 10^{-22}/3.927 \times 10^{-24}$	$m^3$	$V_P = \pi/4d^2l$
Volume of tumor	$V_T$	$1.131 \times 10^{-4}$	$m^3$	Eq. (25)
Number of nanowires	$N$	$1.302 \times 10^{13}/2.604 \times 10^{15}$	...	$N = cV_T/V_P$
Number density	$n$	$1.151 \times 10^{17}/2.302 \times 10^{19}$	$m^{-3}$	$n = N/V_T$
Diffusion length	$\lambda_T$	$7.267 \times 10^{-3}$	$m$	Eq. (28)
Angular velocity	$\omega_M$	$3.142 \times 10^4/6.283 \times 10^3$	$s^{-1}$	$\omega_M = 2\pi f_M$
Time constant diff.	$\tau_D$	$6.104 \times 10^2$	$s$	Eq. (36a)
Time constant perf.	$\tau_B$	$1.623 \times 10^3$	$s$	Eq. (36b)
Time constant	$\tau$	$4.436 \times 10^2$	$s$	Eq. (35)
Spec. heat source nanow.	$\dot{q}_P$	$6.144 \times 10^4$	$W m^{-3}$	Sec. term (33c)
Spec. heat source metab.	$\dot{q}_M$	$1.056 \times 10^3$	$W m^{-3}$	Ref. 49
Total heat source	$\dot{q}$	$6.249 \times 10^4$	$W m^{-3}$	Eq. (33c)
Crit. magnetic field	$H_{0,crit}^*$	$3.681 \times 10^4/4.602 \times 10^4$	$A m^{-1}$	Eq. (20)
Critical exposure	$H_{0,crit}^* f_M$	$1.841 \times 10^8/4.602 \times 10^7$	$A m^{-1} s^{-1}$	$f_M$ in Table II
Steady state temp.	$T_\infty$	$4.300 \times 10^1$	$^\circ C$	Eq. (33b)

## VI. CLINICAL ACCEPTED LIMITS AND THE PRESENTED METHOD

The clinically accepted upper limit of the peak magnetic field and applied frequency for conventional magnetic hyperthermia is described by the medical Atkinson-Brezovich limit:  $(H_0^*f)_{crit} = 5 \times 10^8 A m^{-1} s^{-1}$  (see Ref. 32). This limit on the field-frequency product,  $H_0^*f$ , has been derived from clinical trials on extended time-period thermal impact on the thorax or chest region (see Ref. 50). Since the thermal power  $P$ , dissipated by eddy current heating on healthy tissue, is proportional to the square of  $H_0^*f$  and to the square of the radius  $r$  of the body part to be treated, higher fields can be thermally tolerated in smaller body parts like the arm or the leg as compared to the thorax/chest. Clinical studies and applications of magnetic hyperthermia undertaken in Japan,<sup>33</sup> USA,<sup>34</sup> Chile,<sup>35</sup> and Germany<sup>51</sup> were focused on the frequency range between 50 and 250 kHz and have adhered to the Atkinson-Brezovich threshold as shown in Fig. 10.

At lower frequencies (500 Hz–50 kHz), in addition to eddy-current-based heating of healthy tissues, a further restriction on the peak magnetic field amplitude arises from magneto-stimulation of the peripheral nervous system due to the induced electric field. Data from clinical experiments revealing the perception threshold of some parts of the body, such as the wrist<sup>52</sup> and in arms and legs<sup>53</sup> are also shown in Fig. 10. The magneto-stimulation perception threshold at lower frequencies is below the thermal tolerance set by the Atkinson-Brezovich limit. Finally, for comparison, we also

present the magnetic field occupational exposure limit, defined in the guideline (see ICNIRP<sup>54</sup> and ICNIRP<sup>55</sup>) published by the International Commission on Non-Ionizing Radiation Protection (ICNIRP). In this guideline, limiting curves were determined by applying the safety factor ten. This guideline sets a limit on the amount of exposure to medical personnel and technicians. From the review on the guidelines on magneto-stimulation perception thresholds and eddy-current based thermal limits, it is not so clear whether a strict limit exists for a last-resort intervention therapy like hyperthermia, which is usually applied in cases of advanced cancer, usually along with radiation therapy. However, in such cases, a certain extension of the published limits seems reasonable.

The results of our feasibility study fit well into this diagram. With an overall set of realistic parameters, it is possible to achieve a heating of the tumor up to at least 43 °C. By working with a constant magnetic field at the limiting frequency set by the Atkinson-Brezovich condition, even substantially higher tumor temperatures could be obtained.

## VII. FURTHER DEMONSTRATIONS OF THE APPLICABILITY OF THE MODEL

### A. Introduction to the study of cancers of different geometries

The proposed model consists of several coupled equations, describing the kinematics of the nanowires, their magnetic, fluid dynamic, and thermodynamic behavior

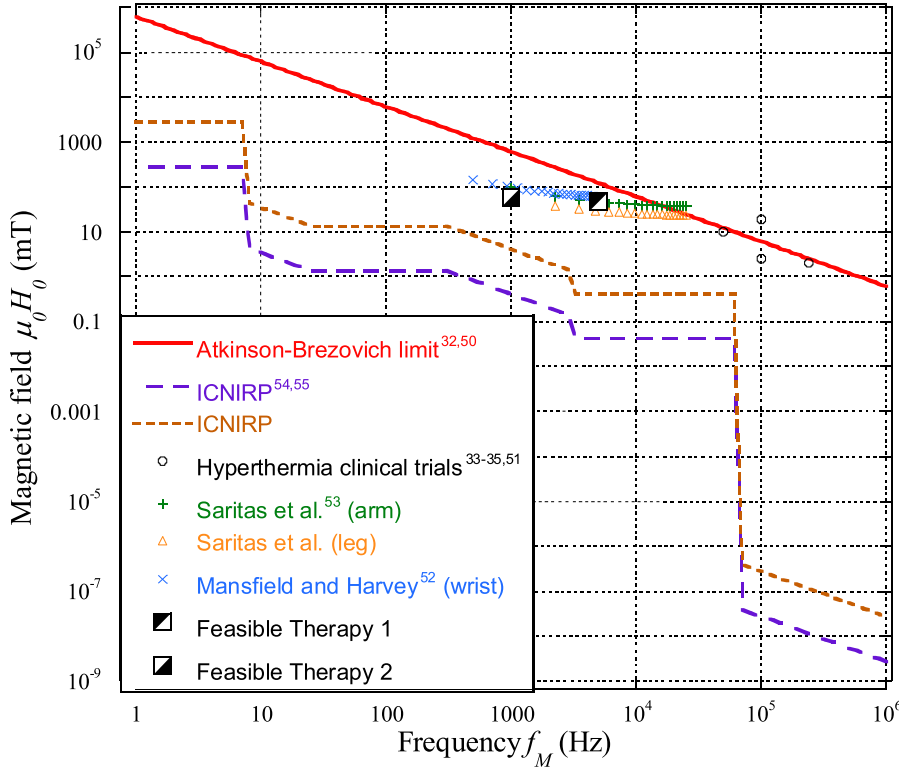


FIG. 10. The medical magnetic-field-frequency diagram containing the well-accepted limit defined by the International Commission on Non-Ionizing Radiation Protection guidelines (ICNIRP) and numerous clinical trials. Our two feasible therapy proposals, FS1 (5000 Hz, 46.3 mT) and FS2 (1000 Hz, 57.8 mT), are well positioned in the domain of tolerated magnetic therapies using alternating magnetic fields.

and also the thermodynamic response of the cancer tumor. Our model formulation, systematically presented in this article, can be easily programmed and numerically calculated. The model allows to model the heating behaviour in various tumor shapes. In addition to the spherical tumor model demonstrated in Sec. IV, we study the influence of two other types of cancer geometries, namely, an oblate spheroid (disk-type) tumor of 60 mm radius and 7.5 mm height and a long prolate (cigar-like) cancer of 21.2 mm radius and 120 mm height. The total cancer volume  $V_T$  remains the same in all three cases. Table V lists the model parameters that are influenced by the three cancer geometries.

**B. Heating performance**

In Fig. 11, we show the impact of the magnetic field and frequency of the method to the spherical cancer tumor’s

TABLE V. The model parameters that are influenced by the spherical, oblate, and prolate tumor geometries are listed. The volume of all three tumors is identical, namely,  $V_T = 1.131 \cdot 10^{-4} \text{ m}^3$ .

Symbol	Unit	Oblate	Sphere	Prolate
$a_T = b_T$	m	$6.000 \times 10^{-2}$	$3.000 \times 10^{-2}$	$2.121 \times 10^{-2}$
$c_T = r_T$	m	$7.500 \times 10^{-3}$	$3.000 \times 10^{-2}$	$6.000 \times 10^{-2}$
$e$	...	$9.922 \times 10^{-1}$	$0.000 \times 10^0$	$9.354 \times 10^{-1}$
$G$	...	$4.360 \times 10^{-2}$	$1.000 \times 10^0$	$3.658 \times 10^0$
$g$	...	$1.565 \times 10^0$	$3.000 \times 10^0$	$6.986 \times 10^0$
$\lambda_T$	m	$4.327 \times 10^{-3}$	$7.267 \times 10^{-3}$	$6.633 \times 10^{-3}$
$\tau_D$	s	$1.741 \times 10^2$	$6.104 \times 10^2$	$4.785 \times 10^2$
$\tau$	s	$1.573 \times 10^2$	$4.436 \times 10^2$	$3.695 \times 10^2$
$T_\infty$	°C	$3.913 \times 10^1$	$4.300 \times 10^1$	$4.200 \times 10^1$
Pn	...	$1.073 \times 10^{-1}$	$3.761 \times 10^{-1}$	$2.948 \times 10^{-1}$
Ti	...	$5.471 \times 10^6$	$1.918 \times 10^7$	$1.503 \times 10^7$
Rs	...	$5.750 \times 10^{-2}$	$1.622 \times 10^{-1}$	$1.351 \times 10^{-1}$

temperature, by extending the field-frequency regime of example FS1. A more than linear increase of the final tumor temperature can be observed towards higher frequencies. By operating at the Atkinson-Brezovich limit, at a frequency of  $f_M = 8200 \text{ Hz}$ , the achieved final tumor temperature in the spherical type cancer is  $\vartheta_T = 50^\circ \text{C}$ . This demonstrates the very high heating performance of this cancer treatment method. However, in this case, it would be recommended to decrease the concentration of nanowires, to target a desired final tumor temperature of  $43^\circ \text{C}$ .

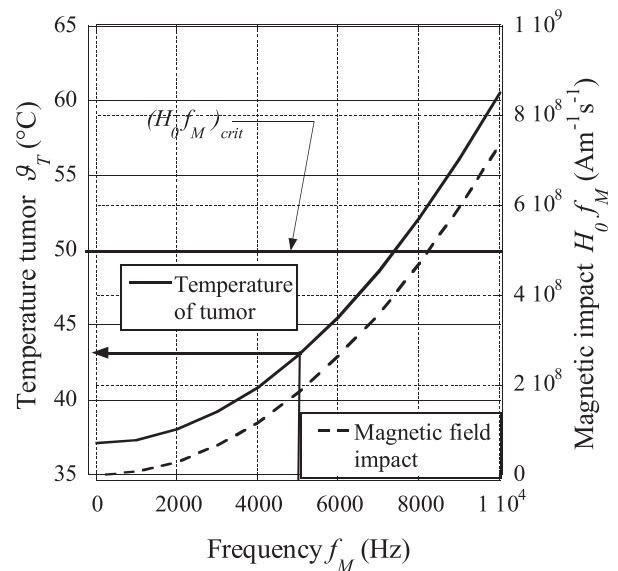


FIG. 11. The final tumor temperature  $\vartheta_T$  increases nonlinearly with increasing rotational frequency,  $f_M$ , of the magnetic field. One can see that our feasibility study FS1, by choosing the frequency  $f_M = 5000 \text{ Hz}$ , easily fulfills the medical requirements, and guarantees heating to the final temperature of the hyperthermia treatment  $\vartheta_T(\infty) = 43.0^\circ \text{C}$ . The volumetric nanowire concentration in this case is  $2.260 \times 10^{-5}$ .

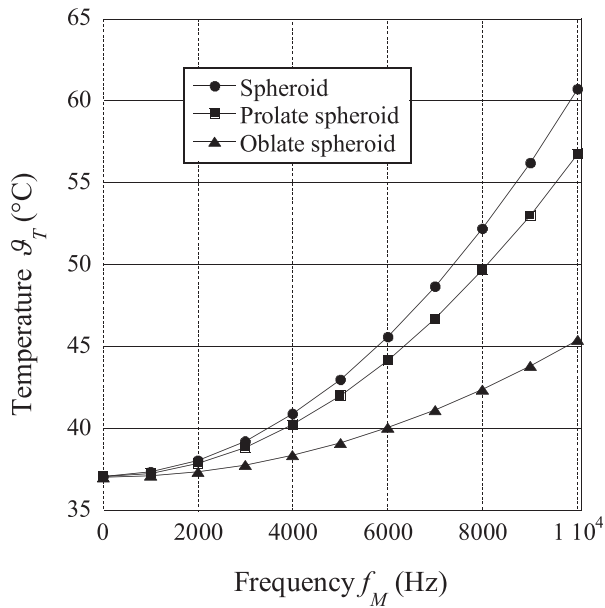


FIG. 12. The heating of a tumor by fluid friction is frequency dependent. Highest heating rates are obtained in spherical tumors, medium rates in prolate, and the lowest rates in oblate spheroids. At frequencies in the range of 5000 Hz, a medium-sized cancerous tumor, with a characteristic diameter of a few centimeters, is sufficiently heated to temperatures that are typically demanded in a hyperthermia cancer treatment.

In Fig. 12, we compare the final tumor temperature across the three tumor geometries (Table V). At 5000 Hz, the spherical tumor heats up and reaches the highest final temperature,  $T_\infty = 43.0^\circ\text{C}$ , while in the prolate spheroid cancer, the final temperature reaches  $42.0^\circ\text{C}$ , and in the case of the oblate spheroid one, temperatures converge to  $39.1^\circ\text{C}$ . By applying  $f_M = 10\,000\text{ Hz}$ , the spherical tumor would reach a temperature of  $60.7^\circ\text{C}$ .

Fig. 13 highlights the tumor geometry dependence of the heating curves. The tumors have an initial temperature  $\vartheta_T(0) = 37.0^\circ\text{C}$ , which is identical to the constant human body temperature. At  $t=0$ , the hyperthermia method is switched on and the magnetic field starts to rotate and forces the nanowires to also rotate with identical frequency. The steady-state temperature reached in the prolate spheroid is higher than in the oblate spheroid. Even though they have the same volume, the prolate spheroid's smaller surface leads to a smaller diffusion heat loss compared to the oblate spheroid. The sphere, which has the maximum volume to surface-area ratio, is the most compact body, and consequently with the heat flux by perfusion and metabolism reaches the highest final temperature. The spherical tumor heats up with a time constant of 7.4 min and after approximately 25 min reaches the therapeutic demanded temperature of  $\vartheta_T(\infty) = 43.0^\circ\text{C}$ . If this transition time is too long, then an initially higher frequency, within the medical tolerated limits, may be chosen to accelerate the heating process. In a clinical hyperthermia cancer therapy, the proposed healing procedure is usually repeated several times.

### C. Dynamical behaviour

In this section, the dynamical behaviour of the hyperthermia method is presented. The time constant is calculated

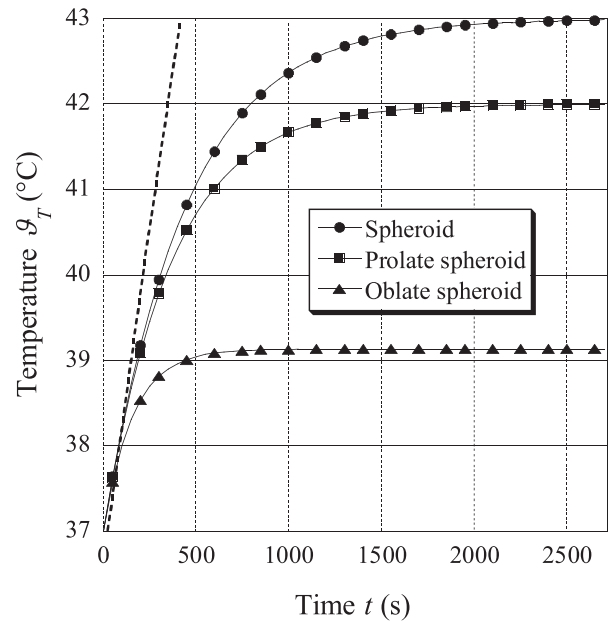


FIG. 13. A comparison of the model results of a spheroid, a prolate, and oblate spheroid each of equal volume, calculated with help of Eqs. (33a)–(33f). The results are explained in the text body of this article; roughly speaking, the final temperature is mainly determined by the area to volume ratio of the related tumor. More specific influences are taken into consideration by the sophisticated diffusion length modelling described by (Eq. (28)).

with Eq. (33d), which in a dimensionless analysis, taking Eqs. (34), (35), and (39) into consideration, leads to the simple form

$$\tau = \frac{Ti}{1 + Pn} \tau_M. \tag{52}$$

The time constant is a material dependent quantity, which here is determined by the characteristics of the tissue. A

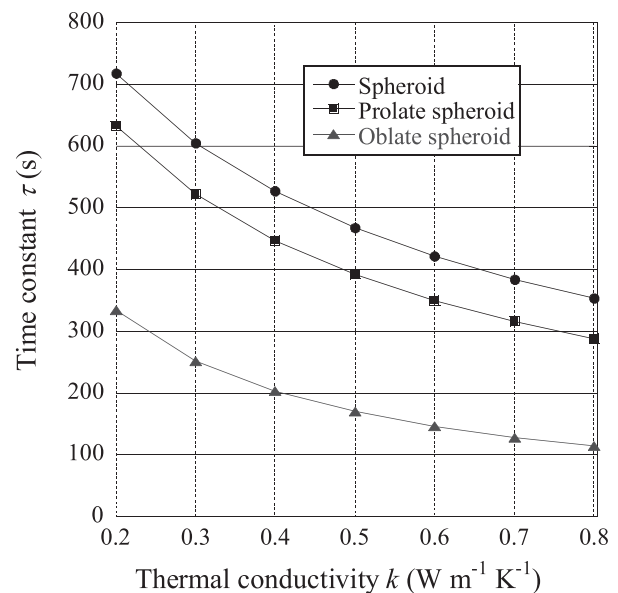


FIG. 14. The time behaviour of a tumor is characterised by its time constant  $\tau$ . In this figure,  $\tau$  is shown as a function of the thermal conductivity  $k_T$ .  $\tau$  decreases with the increase in thermal conductivity.

larger thermal capacity leads to a longer heating time to reach the final temperature level. Since we proposed the injection of nanowires with a biocompatible gel into the tumor, the choice of the gel leaves a certain liberty to obtain appropriate physical properties. It was already mentioned that moderate gel viscosities guarantee the nanowire rotation. Furthermore, the choice of the thermal conductivity influences the time behaviour (time constant) as shown in Fig. 14. The standard value of example FS1,  $k_T = 0.55 \text{ W m}^{-1} \text{ K}^{-1}$  leads to  $\tau = 444 \text{ s}$  in correspondence with the value given in Table IV. The prolate and oblate spheroids show smaller time constants.

#### D. The necessary nanoparticle, respectively, nanowire numbers

To further demonstrate the usefulness of our model, a very practical question is solved, namely, as to how many particles must be injected into a tumour of a given shape and size to obtain a predefined steady-state temperature.

By combining Eq. (33b) with (33c), it follows that

$$T_\infty - T_E = \frac{(\dot{q}_M + c\dot{q}_{P,Mat})\tau}{\rho_T c_{pT}}. \quad (53)$$

By solving this equation, one obtains the particle concentration

$$c = \frac{\rho_T c_{pT}(T_\infty - T_E)}{\dot{q}_{P,Mat}\tau} - \frac{\dot{q}_M}{\dot{q}_{P,Mat}}, \quad (54)$$

and inserting the time constant  $\tau$  from Eq. (27d) leads to

$$c = \frac{\rho_T c_{pT}(T_\infty - T_E)}{\dot{q}_{P,Mat}} \left( \frac{g\alpha_T}{c_T \lambda_T} + \frac{c_{pB}\omega}{\rho_T c_{pT}} \right) - \frac{\dot{q}_M}{\dot{q}_{P,Mat}}. \quad (55)$$

With

$$c = \frac{NV_P}{V_T} \iff N = c \frac{V_T}{V_P} = c \frac{a_T^2 c_T}{a_P^2 c_P}, \quad (56a-c)$$

one obtains the number of magnetic particles  $N$  necessary to reach the final tumour temperature  $T_\infty$

$$N = \frac{V_T}{V_P} \left[ \frac{c_{pB}\omega(T_\infty - T_E)}{\dot{q}_{P,Mat}} \left( 1 + \frac{g\rho_T c_{pT}\alpha_T}{c_T \lambda_T c_{pB}\omega} \right) - \frac{\dot{q}_M}{\dot{q}_{P,Mat}} \right]. \quad (57)$$

This result can be simplified by introducing the Pennes number (37a)

$$N = \frac{V_T}{V_P} \left[ \frac{c_{pB}\omega(T_\infty - T_E)}{\dot{q}_{P,Mat}} \left( 1 + \frac{1}{Pn} \right) - \frac{\dot{q}_M}{\dot{q}_{P,Mat}} \right]. \quad (58)$$

With the specific blood perfusion heat flux at steady-state temperature

$$\dot{q}_B(T_\infty) = c_{pB}\omega(T_\infty - T_E), \quad (59)$$

one derives the following formula:

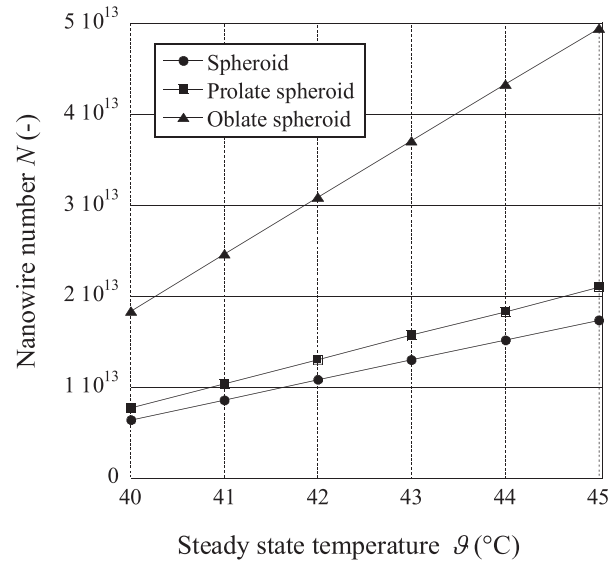


FIG. 15. The particle number  $N$  as a function of the final temperature  $T_\infty$  is shown for the three different tumor geometries. Particle numbers in the order  $10^{13}$  are required to obtain reasonable heating rates.

$$N = \frac{V_T}{V_P} \frac{1}{\dot{q}_{P,Mat}} \left[ \left( 1 + \frac{1}{Pn} \right) \dot{q}_B(T_\infty) - \dot{q}_M \right]. \quad (60)$$

We now recognize the steady-state energy conservation law. By multiplying on the left-hand side  $N$  with  $V_P \dot{q}_P$ , we obtain the heat produced by the nanowires,  $\dot{O}_P$ . On the right-hand side, the first term is the heat flux by perfusion at steady-state temperature. The second is the diffusion heat loss, but with help of the Pennes number expressed in terms of the perfusion value. Finally, the last term to the right is the metabolism term. If the losses (perfusion and diffusion) are high, a high number of particles are demanded. On the other hand, a high metabolism, which also heats the tumour, decreases this demand (negative sign). Furthermore, if the specific heat production in the denominator is small, the number of particles needs to be large and vice versa. In Fig. 15, the particle number is plotted for six steady-state temperatures. Since a strong diffusion effect occurs in plate-like oblate spheroids, the number of particles required for its heating is much higher.

If we assume that no diffusion occurs, then it follows in Eq. (37b) that  $k_T = 0$  and by this also that  $Pn$  is infinite. Under these circumstances, Eq. (60) simplifies to

$$N = \frac{V_T}{V_P} \frac{1}{\dot{q}_{P,Mat}} [\dot{q}_B(T_\infty) - \dot{q}_M]. \quad (61)$$

It is clear that if the sink term for heat described by blood perfusion and the heat source by metabolism is identical, then no particles are necessary to keep the temperature at the level of the human blood temperature. This is the special case of our model in the situation of a human body without a hyperthermia treatment.

#### VIII. CONCLUSIONS

A hyperthermia strategy employing magnetically rotating nanowires is presented. Heat generation is induced by

fluid friction in the boundary layer of the moving nanowires. A kinematical model of nanowire rotation is presented. This physical model is based on a continuum-field-theoretical approach valid for low Knudsen numbers. Furthermore, a coupled fluid and thermodynamic model (which is in certain aspects a generalization of Pennes model) is introduced. The kinematic model is coupled by the heating source term to the thermodynamic model. In combination, they describe fluid friction generated by the rotation of the nanowires.

The combined model allows us to numerically calculate the heating process in a cancer tumor for a variety of parameters. In a feasibility study respecting medical guidelines, two examples of optimal parameter sets are demonstrated, which highlight the efficacy of this method. Finally, a parametric simulation study of heating effects in various tumor geometries and nanowire-gel combinations is performed. The proposed low frequency nanowire-rotation hyperthermia can create high heating rates at small nanowire concentrations.

## ACKNOWLEDGMENTS

We are grateful to L. Gravier and G. Courret for excellent collaboration over the years in the fields of nanotechnology and thermodynamics. S.P. acknowledges funding from the European Research Council's Starting Grant No. 336456.

- <sup>1</sup>R. K. Gilchrist, R. Medal, W. D. Shorey, R. C. Hanselmann, J. C. Parrot, and C. B. Taylor, *Ann. Surg.* **146**(4), 596–606 (1957).
- <sup>2</sup>R. Hergt, W. Andrä, C. G. d'Ambly, I. Higler, W. A. Kaiser, U. Richter, and H. G. Schmidt, *IEEE Trans. Magn.* **34**, 3745–3754 (1998).
- <sup>3</sup>L. Wei-Syuan, L. Hong-Min, C. Hsiang-Hsin, H. Yeu-Luang, and C. Yuh-jing, *J. Nanomater.* **2013**, 237439 (2013).
- <sup>4</sup>D. S. Choi, J. Park, S. Kim, D. H. Gracias, M. K. Cho, Z. K. Kim, A. Fung, S. E. Lee, Y. Chen, S. Khanal, S. Baral, and J. H. Kim, *J. Nanosci. Nanotechnol.* **8**, 2323–2327 (2008).
- <sup>5</sup>L. M. Armijo, Y. I. Brandt, D. Mathew, S. Yadav, S. Maestra, A. C. Rivera, N. C. Cook, N. J. Withers, G. A. Smolyakov, N. L. Adophi, T. C. Monson, D. L. Huber, H. D. C. Smyth, and M. Osinski, *Nanomaterials* **2**, 134–146 (2012).
- <sup>6</sup>R. Zuchini, H. W. Tsai, C. Y. Chen, C. H. Huang, S. C. Huang, G. B. Lee, S. F. Huang, and X. Z. Lin, *Eur. J. Surg. Oncol.* **37**, 604–610 (2011).
- <sup>7</sup>K. Sato, Y. Watanabe, A. Horiuchi, Y. Shungo, T. Doi, M. Yoshida, Y. Yamamoto, N. Tsunooka, and K. Kawachi, *J. Surg. Res.* **146**, 110–116 (2008).
- <sup>8</sup>R. E. Rosensweig, *Ferrohydrodynamics* (Dover Publications, New York, 1997), ISBN: 0-486-67834-2.
- <sup>9</sup>F. Vereda, J. de Vicente, and R. Hildago-Alvarez, *Chem. Phys. Chem.* **10**, 1165–1179 (2009).
- <sup>10</sup>D. H. Kim, D. E. Nikles, D. T. Johnson, and Ch. S. Brazel, *J. Magn. Magn. Mater.* **320**, 2390–2396 (2008).
- <sup>11</sup>L. L. Lao and R. V. Ramanujan, *J. Med. Sci.* **15**, 1061–1064 (2004).
- <sup>12</sup>C. S. S. R. Kumar and F. Mohammad, *Adv. Drug Delivery Rev.* **63**, 789–808 (2011).
- <sup>13</sup>R. E. Rosensweig, *J. Magn. Magn. Mater.* **252**, 370–374 (2002).
- <sup>14</sup>E. Kita, S. Hashimoto, T. Kayano, M. Minagawa, H. Yanagihara, M. Kishimoto, K. Yamada, T. Oda, N. Ohkohchi, T. Takagi, and T. Kanamori, *J. Appl. Phys.* **107**(9), 09B321 (2010).
- <sup>15</sup>E. Zatsepina, A. M. Tishin, and P. W. Egolf, “Magnetocaloric effect applied for a cancer tumor defeat: An improved hyperthermia method,” in *Third IIR International Conference on Magnetic Refrigeration at Room Temperature*, Des Moines, USA, 12–15 May 2009 (Report of a summer internship. Project of Physics Department of the M. V. Lomonosov Moscow State University, Russia and the University of Applied Sciences of Western Switzerland, Thermal Science Institute, Division SIT, 2008), pp. 1–30.
- <sup>16</sup>E. Zatsepina, A. M. Tishin, P. W. Egolf, and D. Vuarnoz, “Magnetocaloric effect applied for a cancer tumor defeat: An improved hyperthermia method,” in *Third IIR International Conference on Magnetic Refrigeration at Room Temperature*, Des Moines, USA, 12–15 May 2009, pp. 487–496.
- <sup>17</sup>E. Zatsepina, “Heat transfer in circulatory system of tumor during treatment process,” Internship in the context of a Master diploma work at the Department of the M. V. Lomonosov Moscow State University, Russia, Supervisor: A. M. Tishin; in collaboration with P. W. Egolf at the University of Applied Sciences of Western Switzerland, Thermal Science Institute, Division SIT, 2009, pp. 1–18.
- <sup>18</sup>R. Hergt, S. Dutz, and M. Zeisberger, *Nanotechnology* **21**, 015706 (2010).
- <sup>19</sup>L. Néel, *C. R. Acad. Sci.* **228**, 664–668 (1949) (in French).
- <sup>20</sup>L. Yang, N. Zhao, and D. Liu, *Adv. Mech. Eng.* **7**(7), 1–11 (2015).
- <sup>21</sup>C. Dennis and R. Ivkov, *Int. J. Hyperthermia* **29**(8), 715–729 (2013).
- <sup>22</sup>H. Mamiya and B. Jayadevan, *Sci. Rep.* **1**, 157 (2011).
- <sup>23</sup>W. F. Brown derived the internal moment relaxation time under an external field in Ref. 24.
- <sup>24</sup>W. F. Brown, *Phys. Rev.* **130**(5), 1677–1686 (1963).
- <sup>25</sup>D. B. Reeves and J. B. Weaver, *Rev. Biomed. Eng.* **42**(1), 85–93 (2014).
- <sup>26</sup>S. A. Shah, D. B. Reeves, R. M. Ferguson, J. B. Weaver, and K. M. Krishnan, *Phys Rev B* **92**, 094438 (2015).
- <sup>27</sup>Here we are not considering the name *relaxation* for the diminishing of transients before a dissipative system reaches its quasi-steady state, which in phase space may be a one- (limit cycle), two- or three-dimensional torus in the case of quasi-periodic movements or may even be a strange attractor in the case of chaotic movements.
- <sup>28</sup>G. Glockl, R. Hergt, M. Zeisberger, S. Dutz, S. Nagel, and W. Weitschies, *J. Phys.: Condens. Matter* **18**, 2935–2949 (2006).
- <sup>29</sup>M. Babinková, D. Leszczynska, P. Sourivong, P. Čičmanec, and P. Babinec, *J. Magn. Magn. Mater.* **225**, 109–112 (2001).
- <sup>30</sup>E. Kita, T. Oda, T. Kayano, S. Sato, M. Minagawa, H. Yanagihara, M. Kishimoto, Ch. Mitsumata, S. Hashimoto, K. Yamada, and N. Ohkohochi, *J. Phys. D: Appl. Phys.* **43**, 474011 (2010).
- <sup>31</sup>P. F. de Châtel, I. Nándori, J. Hakl, S. Mészáros, and K. Vad, *J. Phys.: Condens. Matter* **21**, 124202 (2009).
- <sup>32</sup>W. J. Atkinson, I. A. Brezovich, and D. P. Chakraborty, *IEEE Trans. Biomed. Eng. BME-31*, 70–75 (1984).
- <sup>33</sup>T. Kobayashi, Y. Kida, T. Tanaka, K. Hattori, M. Matsui, and Y. Amemiya, *J. Neuro-Oncol.* **10**, 153–163 (1991).
- <sup>34</sup>B. Stea, J. Kittelson, J. R. Cassidy, A. Hamilton, N. Guthkelch, B. Lulu, E. Obbens, K. Rossman, W. Shapiro, A. Shetter, and T. Cetas, *Int. J. Radiat. Oncol., Biol., Phys.* **24**, 657–678 (1992).
- <sup>35</sup>R. D. Tucker, C. Huidobro, T. Larson, and C. E. Platz, *J. Endourol.* **14**, 511–517 (2000).
- <sup>36</sup>U. Gneveckow, A. Jordan, R. Scholz, N. Waldéfner, B. Hildebrandt, B. Rau, and P. Wust, *Med. Phys.* **31**(6), 1444–1451 (2004).
- <sup>37</sup>H. H. Pennes, *J. Appl. Physiol.* **1**, 93–122 (1948).
- <sup>38</sup>A. Nakayama, F. Kuwahara, and W. Lin, “A general set of bioheat transfer equations based on the volume averaging theory,” in *Porous Media: Applications in Biological Systems and Biotechnology*, edited by K. Vafai (CRC Press, Boca Raton, 2010), Chap. 1.
- <sup>39</sup>B. de Marco, “Magnetocaloric hyperthermia,” Bachelor diploma work at the University of Applied Sciences of Western Switzerland, Yverdon-les-Bains, Supervisor P. W. Egolf, 2013, pp. 1–38.
- <sup>40</sup>W. Bovy, “Nanowires for hyperthermia,” Bachelor diploma work at the University of Applied Sciences of Western Switzerland, Yverdon-les-Bains, Supervisor P. W. Egolf, 2013, 2014, pp. 1–39.
- <sup>41</sup>P. N. Tsague, “Théorie et expériences d’hyperthermie avec des nanofils tournants,” Bachelor diploma work at the University of Applied Sciences of Western Switzerland, Yverdon-les-Bains, Supervisor P. W. Egolf, 2015, pp. 1–60 (in French).
- <sup>42</sup>M. F. Contreras, R. Sougrat, A. Zaher, T. Ravasi, and J. Kosel, *Int. J. Nanomed.* **10**, 2141–2153 (2015).
- <sup>43</sup>B. de Marco, “Hyperthermia cancer treatment with nanowires,” Master diploma work at the University of Applied Sciences of Western Switzerland, Yverdon-les-Bains, Supervisor P. W. Egolf, 2014, pp. 1–22.
- <sup>44</sup>K. Keshoju, H. Xing, and L. Sun, *Appl. Phys. Lett.* **91**, 123114 (2007).
- <sup>45</sup>J. Alonso, H. Khurshid, V. Sanka, Z. Nematii, M. H. Phan, F. Garayn, J. A. Garcia, and H. Srikanth, *J. Appl. Phys.* **117**, 17D113 (2015).
- <sup>46</sup>H. G. Schuster, *Deterministic Chaos: An Introduction*, 2nd ed. (VCH Verlagsgesellschaft mbH, Weinheim, Germany, 1988), ISBN: 3-527-26862-6.

- <sup>47</sup>S. Nakato, K. Miyazaki, S. Izuhara, H. Yamaoka, and D. Tanaka, *J. Phys. Chem. A* **113**, 6876–6879 (2009).
- <sup>48</sup>L. Zhang, T. Petit, Y. Lu, B. E. Kratochvil, K. E. Peyer, R. Pei, L. Nelson, and B. J. Nelson, *ACS Nano* **4**(10), 6228–6234 (2010).
- <sup>49</sup>IT<sup>2</sup>IS Foundation, see <http://www.itis.ethz.ch/itis-for-health/tissue-properties/database/database-summary> for tissue properties database (2014).
- <sup>50</sup>I. A. Brezovich, W. J. Atkinson, and M. B. Lilly, *Cancer Res.* **44**, 4752–4756 (1984).
- <sup>51</sup>K. Maier-Hauff, F. Ulrich, D. Nestler, H. Niehoff, P. Wust, B. Thiesen, H. Orawa, V. Budach, and A. Jordan, *J. Neuro-Oncol.* **103**, 317–324 (2011).
- <sup>52</sup>P. Mansfield and P. R. Harvey, *Magn. Reson. Med.* **29**, 746–758 (1993).
- <sup>53</sup>E. U. Saritas, P. W. Goodwill, G. Z. Zhang, W. Yu, and S. M. Conolly, “Safety limits for human size magnetic particle imaging systems,” in *Magnetic Particle Imaging: A Novel SPIO Nanoparticle Imaging Technique* (Springer, Berlin, Heidelberg, 2012), pp. 325–330.
- <sup>54</sup>ICNIRP, “Guidelines for limiting exposure to time varying electric, magnetic and electro-magnetic fields (up to 300 GHz),” *Health Phys.* **74**, 494–523 (1998).
- <sup>55</sup>ICNIRP, “International commission on non-ionizing radiation protection guideline for limiting exposure to time-varying electric and magnetic fields (1 Hz to 100 kHz),” *Health Phys.* **99**, 818–836 (2009).